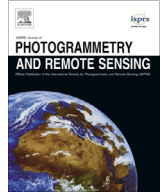




Contents lists available at ScienceDirect

ISPRS Journal of Photogrammetry and Remote Sensing

journal homepage: www.elsevier.com/locate/isprsjprs

Multi-temporal mesoscale hyperspectral data of mixed agricultural and grassland regions for anomaly detection

Cooper McCann^a, Kevin S. Repasky^{b,*}, Rick Lawrence^c, Scott Powell^c^a Physics Department, Barnard Hall Room 264, Montana State University, Bozeman, MT 59717, United States^b Electrical and Computer Engineering, Cobleigh Hall Room 610, Montana State University, Bozeman, MT 59717, United States^c Land Resources and Environmental Sciences, 334 Leon Johnson Hall, Montana State University, Bozeman, MT 59717, United States

ARTICLE INFO

Article history:

Received 21 April 2017

Received in revised form 28 July 2017

Accepted 31 July 2017

Keywords:

Multi-temporal
Hyperspectral
Vegetation
Mesoscale
Anomaly
Classification

ABSTRACT

Flight-based hyperspectral imaging systems have the potential to provide valuable information for ecosystem and environmental studies, as well as aid in land management and land health monitoring. This paper examines a series of images taken over the course of three years that were radiometrically referenced allowing for quantitative comparisons of changes in vegetation health and land usage. The study area is part of a geologic carbon sequestration project located in north-central Montana, approximately 580 ha in extent, at a site requiring permission from multiple land owners to access, making ground based validation difficult. Classification based on histogram splitting of the biophysically based parameters utilizing the entire three years of data is done to determine the major classes present in the data set in order to show the constancy between data sets taken over multiple years. Additionally, a method of anomaly detection for both single and multiple data sets, using Median Absolute Deviations (MADs), is presented along with a method of determining the appropriate size of area for a particular ecological system. Detection of local anomalies within a single data set is examined to determine, on a local scale, areas that are different from the surrounding area and depending on the specific MAD cutoff between 50–70% of the anomalies were located. Additionally, the detection and identification of persistent (anomalies that occur in the same location over multiple data sets) and non-persistent anomalies was qualitatively investigated.

© 2017 International Society for Photogrammetry and Remote Sensing, Inc. (ISPRS). Published by Elsevier B.V. All rights reserved.

1. Introduction

Multi-temporal imaging is a valuable tool for monitoring a multitude of changes over time from land coverage/usage change (Byrne et al., 1980; Lunetta et al., 2006; Rogan et al., 2002) to disease spread (Franke and Menz, 2007; Liangyun et al., 2004; Liu et al., 2006) to urban expansion (Gomez-Chova et al., 2006; Li and Yeh, 1988; Maktav and Erbek, 2005; Xian et al., 2008) and many others (Demirel et al., 2011; Hong et al., 2010; Travelletti et al., 2012; Tripathy et al., 1996). This technique has been driven by free access to high quality satellite data and the long time-frame of operation of these satellites, most prominently Landsat and MODIS. Multi-spectral satellites have dominated the multi-temporal field, but multi-temporal hyperspectral data would allow for further advances in the areas mentioned previously. This paper outlines two uses for multi-temporal radiometrically referenced

hyperspectral data, multi-year classification and single- and multi-year anomaly detection, though the potential uses for radiometrically referenced data are extensive.

While there are several multi-temporal hyperspectral studies utilizing ground based sampling (Lausch et al., 2013; Nguyen and Lee, 2006; Strachan et al., 2002; Stuckens et al., 2011; Xie et al., 2013) this paper focuses on flight-based multi-temporal hyperspectral studies (Franke and Menz, 2007; Liu et al., 2010) of which there are limited examples especially at the mesoscale. With constantly improving technology in terms of the sensors and more advanced atmospheric models there is an ever-increasing array of problems that can be addressed by multi-temporal hyperspectral imaging. A sizable percentage of these problems will require high quality radiometrically referenced data to draw quantitative conclusions. Many multi-temporal studies rely on satellite or flight data that lacks any type of absolute calibration to surface reflectance (Conese and Maselli, 1991; Goenaga et al., 2013; Mallet et al., 2015; Petitjean et al., 2012; Yuan et al., 2015). This approach relies on unchanging atmospheric conditions and that the

* Corresponding author.

E-mail address: repasky@ece.montana.edu (K.S. Repasky).

calibration of the sensor is maintained, limiting the quantitative information that can be obtained.

One specific use of multi-temporal hyperspectral data is monitoring of geologic carbon sequestration sites. Geologic carbon sequestration (Li et al., 2006; Zhang et al., 2002) provides a means of capturing carbon dioxide (CO₂) (Cuffey and Vimeux, 2001; Monnin et al., 2001; Pachauri and Reisinger, 2007; Petit et al., 1999; Siegenthaler et al., 2005) at a facility such as a power plant and storing this captured CO₂ underground in geologic formations. The stored CO₂ is removed from the atmosphere providing a mitigation technique for CO₂ emission directly to the atmosphere. Successful carbon sequestration requires the development of a variety of technologies including carbon capture, understanding the storage capacity and safety of the various geologic formations (Benson et al., 2004; Cortis et al., 2008; Knauss et al., 2005; Oldenburg et al., 2009; Pruess, 2008; Wilson et al., 2007), and monitoring and verification technologies (Spangler et al., 2010; Strazisar et al., 2009) and techniques to ensure the efficacy of the carbon sequestration site. Monitoring and verification technologies need to be able to efficiently monitor the large areas associated with carbon sequestration sites, which are on the order of tens to hundreds of square kilometers (Rutqvist et al., 2010; Korbøl and Kaddour, 1995; Whittaker, 2004; Maldal and Tappel, 2004).

Airborne remote sensing is one technique proposed for monitoring the large areas associated with carbon sequestration sites. Flight based hyperspectral imaging has the potential to monitor vegetation for signs of stress that may be associated with water deficiency (Behmann et al., 2014; Dobrowski et al., 2005; Jones et al., 2004; Kim et al., 2011; Suárez et al., 2008; Tilling et al., 2007; Zhao et al., 2005), nitrogen deficiency (Strachan et al., 2002; Tilling et al., 2007; Zhao et al., 2005), and elevated CO₂ in the soil (Bateson et al., 2008; Bellante et al., 2013; Bergfeld et al., 2006; Keith et al., 2009; Maček et al., 2005; Male et al., 2010; Noomen et al., 2008; Noomen and Skidmore, 2009; Pickles and Cover, 2004), or other types of stress (Apan et al., 2004; Dobrowski et al., 2005; Smith et al., 2004; Zhang et al., 2003). Remote sensing-based surveys of carbon sequestration sites by flight based hyperspectral imaging can then be used to direct more expensive, time consuming, and resource intensive sensors (such as hand-held CO₂ sensors) to potential problem areas.

Hyperspectral imaging systems provide a reflectance spectra for each pixel in the digital image. Low-cost hyperspectral imaging systems can provide reflectance spectra in the 400–950 nm spectral range containing important spectral features associated with vegetation including the low spectral reflectance in the visible associated with absorption of the chlorophyll, the rapid rise in the reflectance spectra between 700 nm and 800 nm often referred to as the red-edge, and the high spectral reflectance in the near infra-red (IR) associated with the leafy mesophyll.

Elevated CO₂ levels in the soil can cause stress in vegetation which can manifest in changes in the spectral reflectance. Stress causes a reduction of the photosynthetic pigments which results in an increase in visible portion of the reflectance spectra (Carter et al., 1992; Knipling, 1970). Furthermore, stress affects the internal structure of plant cells that decrease the reflectance spectra in the near-IR portion of the reflectance spectra (Carter, 1991; Knipling, 1970; Li et al., 2005). Both effects could be used as an early indicator of stressed vegetation (Carter and Knapp, 2001; Luther and Carroll, 1999; Eitel et al., 2011). The changes in the reflectance spectra resulting from vegetation stress can be monitored via flight-based hyperspectral imaging. In particular, a time series of flight based hyperspectral images, either from aircraft, unmanned aerial vehicles (UAV's), or drones, will allow the monitoring of the evolution of vegetation stress over the course of a growing season and/or from year to year.

Initial experiments demonstrating the ability of hyperspectral imaging to detect stressed vegetation were conducted during controlled sub-surface release experiments at the Zero Emission Research Technology (ZERT) field site. Detecting vegetation stress using a ground based hyperspectral instrument has been demonstrated (Keith et al., 2009). Subsequent work by Bellante et al. and others (Bellante et al., 2013; Male et al., 2010; Pickles and Cover, 2004; Spangler et al., 2010), also performed at the ZERT field site, demonstrated the ability of a flight based hyperspectral imaging system to detect the evolution of the vegetation stress resulting from a sub-surface release. During this experiment, eight flights were conducted over the ZERT field sites, and data was collected over an area of approximately 1 ha. Georeferencing corrections were achieved using ground based targets that could have been used for atmospheric correction as well.

Initial demonstrations of hyperspectral imaging indicate that it is a viable method of monitoring carbon sequestration sites. Recent work (McCann et al., 2017a) has demonstrated the ability to use U.S. Geological Survey (USGS) 0.3 m resolution orthoimages for georectification and the Landsat 8 surface reflectance data product to produce radiometrically referenced large area hyperspectral images with minimal ground access. Furthermore, a method of fitting reflectance spectra with basis functions based on biophysically relevant fit parameters as a means of data and noise reduction (McCann et al., 2017a) has been demonstrated. Additionally, using these fit parameters, an unsupervised classification technique based on histogram splitting of the fit parameters has been demonstrated (McCann et al., 2017a).

This paper looks at three georectified, surface reflectance referenced data sets from hyperspectral imaging flights conducted on 06/21/2014, 06/24/2015, and 06/26/2016 at the Big Sky Carbon Sequestration Partnership (BSCSP) site in north-central Montana. This data is examined using an unsupervised classification technique based on biologically relevant fit parameters, the results are used to look at changes in land usage throughout the time series. Additionally, these clusters can be used in determining large scale management areas or as inputs to a supervised classification technique as a training data set. A method of local anomaly detection is presented using Median Absolute Deviations (MADs). These local anomalies were used as a proxy for detection of a CO₂ leaks. If CO₂ was present in the soil in higher concentrations than the surrounding area the vegetation would appear stressed and appear different spectrally and would be detected as a local anomaly. These anomalies may also be related to different levels of stress within a plant species, different species within the same area (such as weeds in an agriculture field), different land use, soil differences (such as a saline seep), etc. To better isolate local anomalies of interest multiple data sets were compared to eliminate anomalies that are present in the same location across multiple data sets. This isolates anomalies that have developed (or become more anomalous) between data sets indicating a local change that in the case of a CO₂ sequestration site might be an indicator on a leak, which would warrant further investigation.

2. Materials and methods

2.1. Study area and imaging system

The primary study area (N48°51'43", W111°44'10", elevation 1143 m) was located in north-central Montana at the Big Sky Carbon Sequestration Partnership demonstration shown in Fig. 1. The region of interest examined herein, the northern most region, Site C, outlined in green in the inset of Fig. 1, was approximately 580 ha, and contained regions of fallow fields, planted wheat/barley fields, grassland, arroyos, draws, and some buildings and roadways.

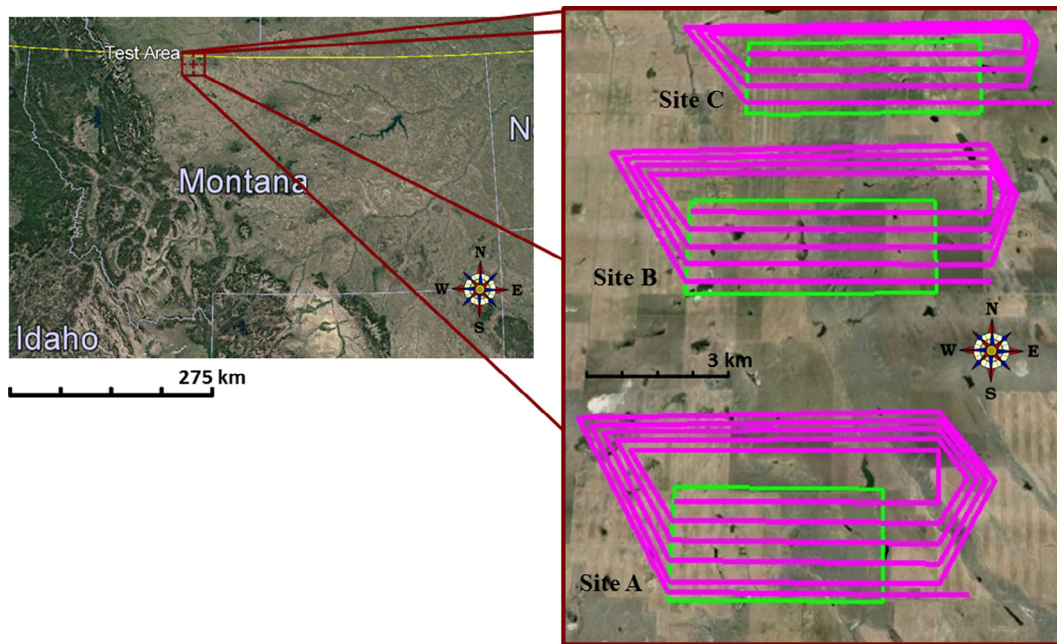


Fig. 1. Location of the Big Sky Carbon Sequestration Partnership (BSCSP) demonstration site in north-central Montana. Inset: Map of the 3 test areas (green) and flight paths (magenta) at the demonstration site.

The hyperspectral imaging system used for data-collection consisted of an imaging spectrometer, a global positioning system/inertial navigation system (GPS/INS), and a flight computer all mounted on a custom-built aluminum plate and flown in a single-engine Cessna Skyhawk. The imaging spectrometer (Pika II from Resonon, Inc., Bozeman, MT, USA) had a spectral range of 425–925 nm, and was binned to provide 80 spectral channels with 6.39 nm spectral resolution. The GPS/INS (Micro INS, MIS-100-000 from Rockwell Collins, Cedar Rapids, IA, USA) provided 0.2° pitch and roll accuracy. Hyperspectral data and GPS/INS data were transferred to a flight computer (P-CAQ PC-104 from Resonon, Inc., Bozeman, MT, USA) for later retrieval. Flights, shown in magenta in the inset of Fig. 1, were made 1220 m above ground level with a 22.5° field of view lens on 06/21/2014, 06/24/2015, and 06/26/2016. Data was taken in a push broom configuration that captured all spectral information in a single instant of time across an entire line perpendicular to the flight direction. Each line captured 640 pixels over 485 m, providing a 0.75 m cross-track resolution. The number of passes was chosen so that, even with the presence of slight turbulence, there would be an overlap between adjacent swaths of 100–150 m. This allowed adjacent swaths to be referenced to each other and guaranteed complete coverage of the test area. For the area examined in this paper, Site C in Fig. 1, four separate flight passes were flown with all data acquired from east-to-west to reduce issues associated with different look angles, which produced four swaths that needed to be combined/mosaicked to produce the final hyperspectral data.

Initial data processing was completed using a technique that combined individual swaths to form a high-resolution multi-swath radiometrically corrected image (McCann et al., 2017a). Briefly, post-processing software (GeoReg Resonon, developed for Resonon, Inc. by Space Computer Corporation (SCC), Los Angeles, CA, USA) was used to geocorrect the imagery using vector tracing algorithms. Then user input was necessary to geocorrect each individual swath to a master 0.3 m orthoimage, yielding an accuracy of less than 2 m RMSE per swath. This accuracy will be one of the limiting factors when comparing data sets from multiple years and could be improved with more advanced instrumentation or with

ground references if available. After this spatial processing, swath-to-swath radiometric correction was performed so that the individual swaths could be mosaicked together. Atmospheric effects were removed using a simple atmospheric model before being radiometrically referenced to the Provisional Landsat 8 Surface Reflectance (LaSRC) data product to create a large-area high-resolution radiometrically referenced hyperspectral image (McCann et al., 2017a).

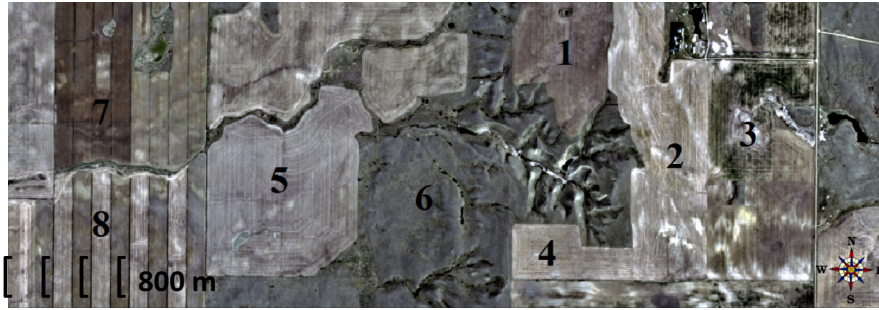
2.2. Field reference data

As with many restricted-access sites, information about specific land use was limited. For this work restricted-access refers to the need for permission from multiple land owners to access the site, but could also refer to wilderness areas, military areas, or other inaccessible land. The self-reported land use provided by landowners is detailed in Fig. 2. Limited site access was obtained in 2015 for fields 2 and 3. This was the only site access during the study years and consisted of visual observations and photographs only.

Additionally, historical rainfall data was obtained for the area from the National Resources Conservation Services (NRCS) for Shelby, MT (Station 7500, 48°30'N, 111°51'W, elevation 1003 m) located approximately 55 km from Site C. No other stations that monitor rainfall and had data for this time period were near the site.

2.3. Classification

Classification was performed using an unsupervised histogram splitting classification method based on biophysically based parameters (McCann et al., 2017b) on all three data sets. In this method, each individual pixel is fit using a set of biophysically relevant basis functions having 9 parameters associated with it. The reduction from 80 spectral bands to 9 parameters provides data reduction as well as noise reduction, but more importantly re-expresses the data in a more physically meaningful way. The biophysically relevant basis functions used consist of two distinct functions, referred to as the red edge and the green peak, that



	Field 1	Field 2	Field 3	Field 4	Field 5	Field 6	Field 7	Field 8
2014	Fallow	Barley	Barley	Fallow	Barley	Grassland	Fallow*	NR
2015	Spring Wheat	W: Fallow E: Barley	Barley	Spring Wheat	Barley	Grassland	NR	Fallow*
2016	Fallow	Barley	Barley	Fallow	Field Peas	Grassland	NR	NR

*Determined based on visual examination, not used for analysis.

NR is Not Reported by landowner, but containing some type of vegetation, not used for analysis.

Fig. 2. Map of Site C with field labels and corresponding table of land use as reported by the land owners for the 3 years under investigation.

are summed to give the final modeled reflectance spectra. The equations for the red edge basis function is

$$RE(\lambda_{HS}) = R2 * \left[\frac{\tan^{-1}((\lambda_{HS} - R3) * R4 * e^{\frac{(\lambda_{HS}-R3)^2}{R5}})}{\pi} + \frac{1}{2} \right] + R1 \quad (1)$$

and defines the baseline reflectance in the visible, the location and behavior of the red edge, and the strength of the near-IR reflectance. The green peak basis function is

$$GP(\lambda_{HS}) = G1 * G4 * e^{\frac{(G3+G4)^2}{2}(\lambda_{HS}-G2)*G4} * normcdf\left(\frac{\lambda_{HS}-G2}{G3} - G3 * G4\right) \quad (2)$$

and defines the characteristics of the green peak found in the visible region. The parameters are described briefly in Table 1 in terms of their meaning/effects.

Each data set has 9 parameters associated with each pixel, so the classification was done on the full 27 parameters (9 parameters per year for each of the 3 yearly data sets). During the classification, a parameter is chosen and a histogram is generated for that parameter. Certain parameters will exhibit peaks in the histogram that can be easily separated forming into natural clusters. The unsupervised classification scheme looks for a parameter with sep-

Table 1
Description of parameters associated with biophysically relevant basis functions used in the fitting of the reflectance spectra of individual pixels.

Name	Description
R1	Baseline in the visible portion of the spectra
R2	Difference between the visible baseline (R1) and the level of the near-IR
R3	Location, in wavelength, of the inflection point of the arctan function, and therefore the location of the red edge
R4	Steepness of the edge of the arctan function is in terms of reflectance versus wavelength
R5	Changes the curvature of the arctan symmetrically near its minimum and maximum
G1	Related to the total area of the green peak
G2	Location of the green peak in wavelength
G3	Width of the green peak
G4	Exponential modifier that gives rise to the 'tail' of the otherwise Gaussian peak and causes a shift towards the red in the apparent green peak location

arable peaks to do an initial split into clusters. Once this is done, within each cluster parameters are examined until another parameter with separable peaks is found. This new parameter is used to split the cluster into further subclusters. This process is repeated multiple times generating a clustered image that does not possess any further natural splittings and can be classified or analyzed as desired (McCann et al., 2017b).

Specifically, this classification on the full set of 27 parameters resulted in less than 10 dominant clusters and approximately 100 minor clusters. Dominant clusters are clusters that contain more than 4% of the total area, minor clusters are the clusters that contain less than 4% of the total area. This cutoff was determined based on visual inspection of the sizes of individual clusters and may differ for other areas. Dominant clusters were analyzed for their behavior over the 3 data sets.

2.4. Single data set anomaly detection

Within a single data set it is possible to map local anomalies based on how different the parameters for a given pixel are from the surrounding pixels (Makki et al., 2017; Zhao et al., 2016). The map of the anomalies is based on the number of Median Absolute Deviations (MADs) for each parameter for a given pixel area surrounding the center pixel being examined. The total MAD for each pixel is the sum across all 9 parameters. MAD is defined as the median of the absolute deviations from the median, or $MAD = median(|X_i - median(X)|)$, and is a robust measure of the variability of a sample of quantitative univariate data (Howell, 2014; Leys et al., 2013). Determining the spatial extent for the area in question was a compromise between including large areas, thereby better representing the behavior of the local area, the processing time required, and the relative change when moving to larger pixel area. For this work, the percent change between different sized pixel areas was minimized at 41×41 pixels, as shown in the upper right graph of Fig. 3. While the most appropriate pixel area will depend on the spatial resolution of the data and the particular ecological system being studied 41×41 pixels will be used for this work. This choice of pixel area is further justified by the plots in Fig. 3. The upper left graph of Fig. 3 shows a histogram of the total MAD across all 9 parameters versus the percentage of occurrences for different sized areas ranging from 11×11 to 61×61 pixels. As the pixel area increases the change in the histograms decreases relative to the next smallest size and the peaks shift towards

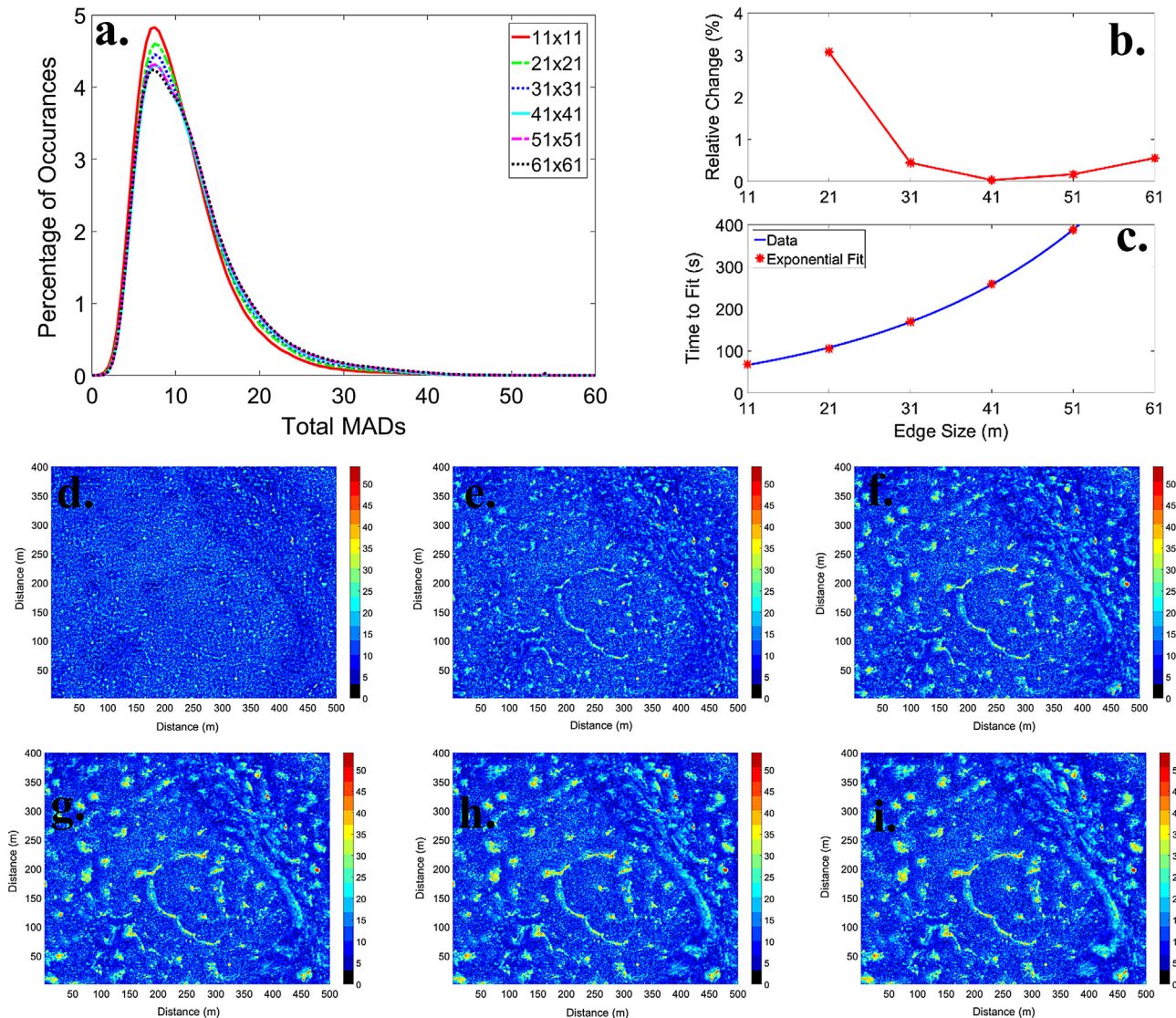


Fig. 3. a: Histogram of the total MAD across all 9 parameters at different sizes areas. b: Relative Change, in percent, between different Edge Sizes showing the small change at 41×41 . c: Time (based on fitting a 501×501 pixel area on a 3×3 GHz processor) versus Edge Size showing the exponential increase with larger sizes. d–i each oriented North-Up: Example area at different sizes areas: 11×11 , 21×21 , 31×31 , 41×41 , 51×51 , and 61×61 . Z-axis is total MADs, larger numbers are more anomalous in relation to surrounding area.

larger MADs. This diminishing return with larger areas coupled with the upper right graph showing an exponential increase in processing time as the area increases and the relative change between different sizes being minimized at 41×41 pixels leads to the choice of using the 41×41 pixel size to represent the local area. Qualitatively this choice can be seen by looking at an area believed to be the boundary to a region that only has water a portion of the year. This area is shown in the plots in the middle and lower rows of Fig. 3. Anomalous areas were visually well distinguished using the 41×41 pixel area as compared to smaller areas, and as the area increased the difference in appearance compared to the next smallest size was minimal.

The deviations, as noted by the high MADs (colors away from blues towards yellow then red on the color bar), from the surrounding may be due to different levels of stress within a plant species, different species within the same area, different land use, soil differences, and other possibilities as well. A CO_2 leak would manifest itself as a plant stress initially, especially in agricultural land that are uniformly planted with a single plant species.

2.5. Multi-data set anomaly detection

With radiometrically referenced (or radiometrically calibrated) data it is possible to track changes based on having knowledge of the end members in an area (Lucas et al., 2007; Somers and Asner, 2012, 2013) or past members (Feitosa et al., 2009). This type of analysis only required radiometrically consistent data as it is not strictly necessary to maintain the same end member library for each set of data. This could be due to imperfect sensor calibration, but more likely would be affected by the natural variation in the reflectance spectra during various stages in its life cycle. This variation can be considered by determining the end members based on the changes over the course of the entire data set (Hemissi et al., 2013).

It is also quite common to utilize invariant sites for calibration (Gevaert et al., 2015; Kerekes et al., 2006; Ong and Cudahy, 2002; Zarco-Tejada et al., 2005). This method works well if the invariant sites are distributed throughout the area and the illumination does not change during data collection (such as from a passing cloud).

To ensure invariant sites, access is required at multiple times (ideally before each flight) to ensure that the sites are truly invariant and not covered with dust, vegetation, or some other contaminant that could change the spectra. Pseudo-invariant targets remove much of this difficulty if available and properly spatially distributed (Hadjimitsis et al., 2009).

The extension of looking at a single data set to multiple data sets can be as simple as subtracting one map from another (Yuan and Elvidge, 1996). If the spatial registration between the images is good then the difference in the total MADs between the data sets will be a measure of the increase/decrease of how anomalous a pixel is in relation to the surrounding area. Large increases in the MAD point to an area that has increased vegetation stress relative to the surrounding area, which might be related to either a CO₂ leak or some other localized environmental change. This is just one simple means of utilizing the temporal component of the hyperspectral data.

3. Results and discussion

3.1. Dominant cluster analysis

The histogram splitting method returned a cluster map of approximately 250 clusters as seen in Fig. 4. With the limited field reference data available, it is possible to broadly assign behaviors to the clusters as shown in the table in Fig. 4. These behaviors are indicative of the broad scale land use and could be used to determine management areas.

Depending on the scientific question under investigation it may be necessary to merge clusters either manually, using an automated algorithm, or by defining management areas. However, here the choice has been made to look at the dominant clusters for the large-scale behavior. This assumes that the dominant clusters are representative of the large-scale behavior of the landscape. This conjecture is based on Fig. 5 that shows the relative percentage of the total area of each cluster. There are 6 clusters that encompass approximately 64% of the study area and are shown in Fig. 6. These dominant clusters could also be used as training data for a supervised classification method as well.

Examination of each dominant cluster gives the spectral plots in Fig. 7. Plots 7a and 7b are produced from the biophysically relevant parameters used to fit the spectra of each pixel and therefore show the noise reduction achieved by using basis functions. Plots 7c and

7d are shown for comparison and contain the original 80 spectral bands. Focusing in on cluster 2, and looking at the spatial location it can be seen that they are located primarily in the field labeled 5 in Fig. 3. This field was reported to contain Barley in 2014, Barley again in 2015, and Yellow Field Peas in 2016. If environmental conditions were the same it would be expected that the spectra from 2014 (solid lines) and 2015 (dotted lines) would be very similar, but this is not the case. The spectra in 2015 is higher in the visible, and slightly lower in the near-IR. This type of change is a common indicator of plant stress (Carter et al., 1992; Carter and Young, 1993; Carter and Knapp, 2001; Chapin, 1991). Upon examination of the historical rainfall for this area there is evidence that 2015 was a dry year as compared to 2014, as shown in Fig. 8. This lack of moisture could be the cause of this stress. However, the grassland, area 6 and cluster 3, do not show this relative stress between 2014 and 2015, and in fact are very uniform through all three years. Since the field was not allowed a fallow year between plantings this relative stress could be due to depleted soil nutrients, or it could simply be due to grasslands being better suited for the environment and being less affected by the dry year.

3.2. Single data set anomaly map

A map of suspected anomalies for a single data set, taken in 2015, is shown in Fig. 9. Gullies are observed as anomalies in the otherwise uniform grassland as they contain vegetation that is greener than the surrounding native grasses as well as water, as seen in Fig. 10 (Left). Also, the rows between the fallow planting rows appear as anomalies, most likely due to residual vegetation that was not tilled when the field was left fallow for the year, as qualitatively identified in the hyperspectral data. The final area to point out is on the east edge, field 3, where barley has been planted contained a saline seep that made growing conditions less than ideal in the surrounding area. Field 3 had large weeded areas throughout, Fig. 10 (Middle), and stunted vegetation, Fig. 10 (Right), which were observed as anomalies in Fig. 9.

There are three areas that are worth noting specifically in this anomaly map. The first is a location of an oil well (API #25101072270000) (Wells Search, 2017) with the surrounding soil being barren shown in Fig. 11 (Left). The second area is located near the oil well and is where when the field was being seeded the seeder stopped before the edge either due to running out of seed or from a slight GPS misalignment. This area seen in Fig. 11

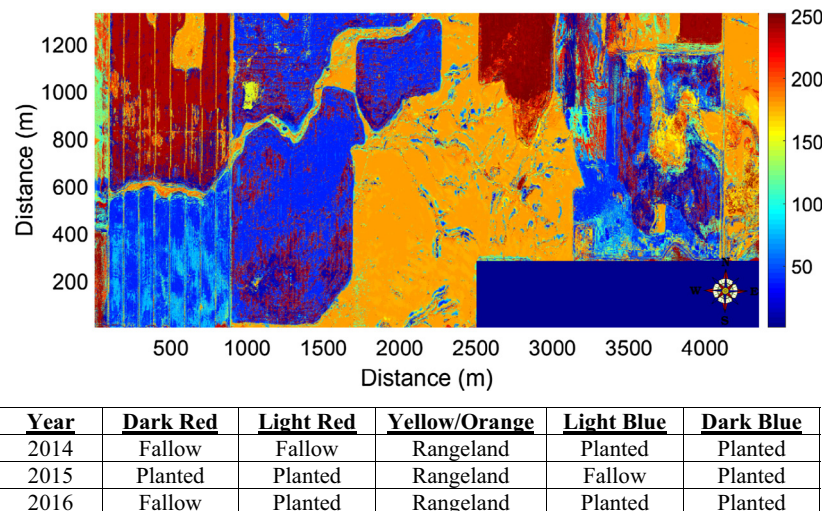


Fig. 4. Histogram based classification using 3 years of biophysical parameters as inputs for a total of 27 parameters, vertical color bar corresponds to cluster number. Table shows roughly how color corresponds with land use over the three years.

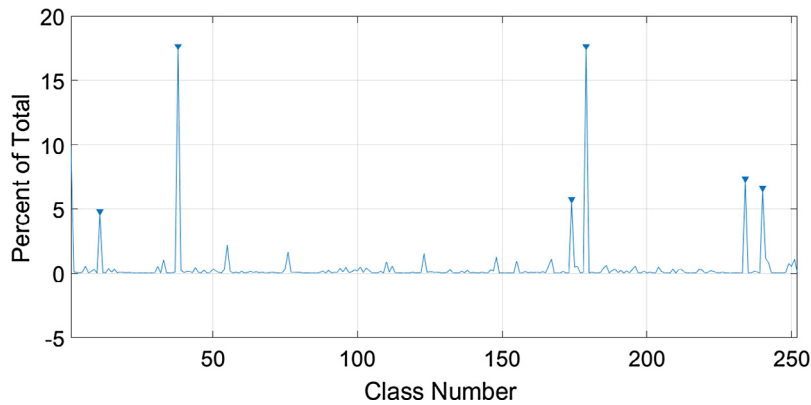


Fig. 5. Relative percentage of individual clusters, here 6 clusters make up approximately 64% of the study area, and if numerically similar classes are included approximately 68% of the study area is included.

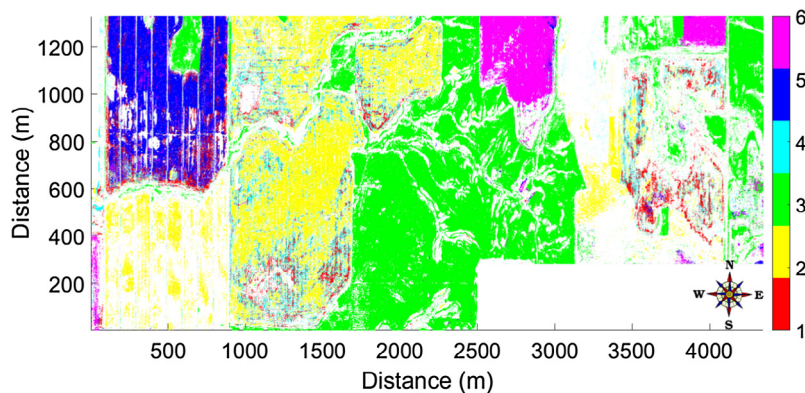


Fig. 6. Dominant clusters. Most of the clusters are constrained to field boundaries and appear to be representative of the large-scale behavior of areas noted in Fig. 3.

(Left) is of the same scale as the local area under consideration (41×41 pixels) and shows up as a barbell shape. The third area was mentioned previously and consisted of numerous weed patches in a barley field (southern portion of Field 2) and also a nearby saline seep shown in Fig. 11 (Right) qualitatively identified during the limited site access to this area.

The oil well is expected to be a persistent anomaly that will appear in every data set. The nearby area that was missed when seeding should be an anomaly that is only present for a single growing season. The size of the saline seep may change depending on the rainfall for the season though the location will be fixed. Finally, the weeded areas are expected to vary in size from year to year if the field is not sprayed, and if sprayed there may be other patches in different areas.

While a single data set can detect local anomalies, some that can be positively identified, a single data set has limited utility because many of the anomalies will be present in multiple data sets. However, with radiometrically referenced data it is possible to examine multiple data sets to remove these persistent local anomalies and focus solely on new local anomalies that may result from the CO_2 leak. With enough temporal resolution, easily obtainable with this type of flight-based system, it would be possible to focus solely on temporal anomalies, but since this work consisted of data separated by one year the focus was on spatial anomalies.

3.3. Single data set accuracy assessment

To evaluate the accuracy of the technique, a small sample area was chosen with features that could be identified as anomalies. The MAD technique was compared to these anomalies to

determine the accuracy of determining these anomalies as well as the amount of areas that were found that are not considered anomalies. Fig. 12a shows a 500×500 m area of state land consisting primarily of grasses with small bushes and rock outcrops throughout. These bushes are labeled as anomalies along with shallow gully features and boundaries of seasonal ponds. Fig. 12b shows the accuracy of the MAD method in finding the anomalies in 12a as well as the percent of the anomalies found by the MAD method that are not considered anomalies in 12a. From Fig. 12b it can be determined that a value of around 15–35 MADs can locate anomalies with a 50–70% accuracy, though at the expense of over finding anomalies by approximately 70%. Most of the anomalies that were missed by the MAD technique were around the areas of dense anomalies such as the upper right portion of Fig. 12a. The MAD technique does not see these areas as spatially anomalous since they are larger than the pixel area being investigated. Over found areas can be attributed to extending beyond the boundaries of the anomalies in Fig. 12a. Finally, looking at Fig. 12d there is evidence that MAD values below 30 are primarily background and above the values are the anomalies. Using this values of 30 as the cutoff for classifying a pixel as anomalous is an appropriate choice for this data set, though for other systems the value will be different.

3.4. Multi-data set anomaly map

One of the most basic approaches in comparing data sets is to take the difference between the individual anomaly maps. This generates a map that shows how much a given area has changed relative to its surrounding area. This is particularly useful for

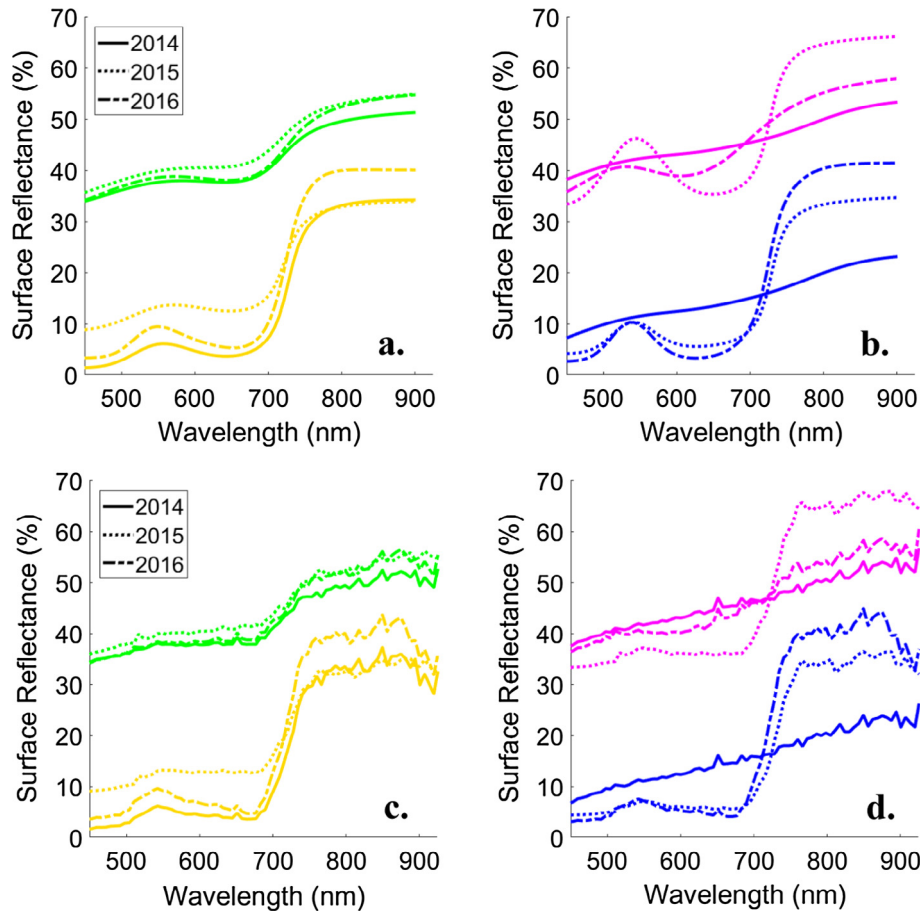


Fig. 7. Mean reflectance spectra of parameters, (a and b), and spectral bands, (c and d), for selected dominant clusters based on biophysical parameters, colors correspond to the same areas in Fig. 6. Data is offset by 30% for clusters 3 and 6 for clarity.

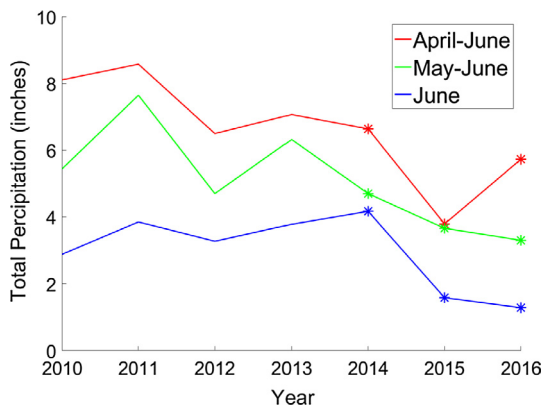


Fig. 8. Historical Monthly Rainfall for Shelby, MT obtained from the NRCS. Precipitation data marked with asterisk are when hyperspectral data was obtained at the end of June. 2015 had markedly less rainfall than 2014.

agricultural areas where the land cover changes dramatically from one year to the next or between plantings during a single growing season. Areas that are more anomalous, either because they are new or because they have become even more different from their local environment, can be considered as new anomalies. A small subset of this type of map is shown in Fig. 13 where for better visualization a cutoff of 10 MADs is imposed and anomalies smaller than 50 m² have been removed. This means that areas in red are more than 10 MADs different in 2016 than in 2015. The opposite

is true of regions in green, they were more different in 2015 than in 2016. Finally, black are regions are not different enough between the data sets to appear as anomalies.

There are some weaknesses to this approach such as the road that shows up as an anomaly when it runs between two planted fields, but not when only one of the fields is planted. This type of anomaly would be improved as more data are analyzed or if known areas such as roads and buildings were masked out before analysis. Similarly, anomalies between planting rows (or fallow rows) in the field in the lower left are seen due to the farmer consistently planting in the same rows. Edges of these rows are consistently fallow (or sparsely vegetated) as compared to between the rows being vegetated so depending on whether the fields are planted these edges may or may not show up as anomalous.

Looking specifically at the positively identified anomalies described previously, namely the oil well, the unseeded region, the saline seep, and the numerous weed patches, as test cases for the technique a number of conclusions can be drawn. On initial examination, the location of the oil well appears to have grown and moved as evidenced by the green and red crescent shapes in Fig. 13. If the area grew or shrank there would be a single colored circular shape, and if were purely movement (such as imperfect spatial registration) the crescents would be the same size. This apparent change in size can be attributed to in 2015 the barren area was compared to a barley field that had a young crop present so many of the individual pixels still contained a strong signal from the soil that would make the area less different than the surrounding as compared to 2016 when it is compared to a lush pea crop.

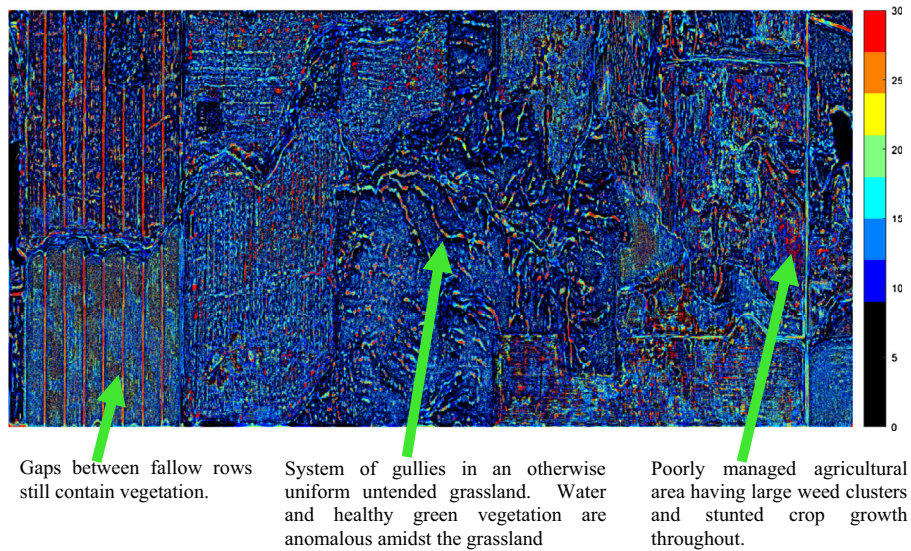


Fig. 9. Anomaly map for data taken in 2015. Vertical color scale corresponds to the number of median absolute deviations a pixel is from the median of the surrounding 41×41 pixel region, summed over all 9 biophysical parameters. Larger numbers are more likely to be anomalies.

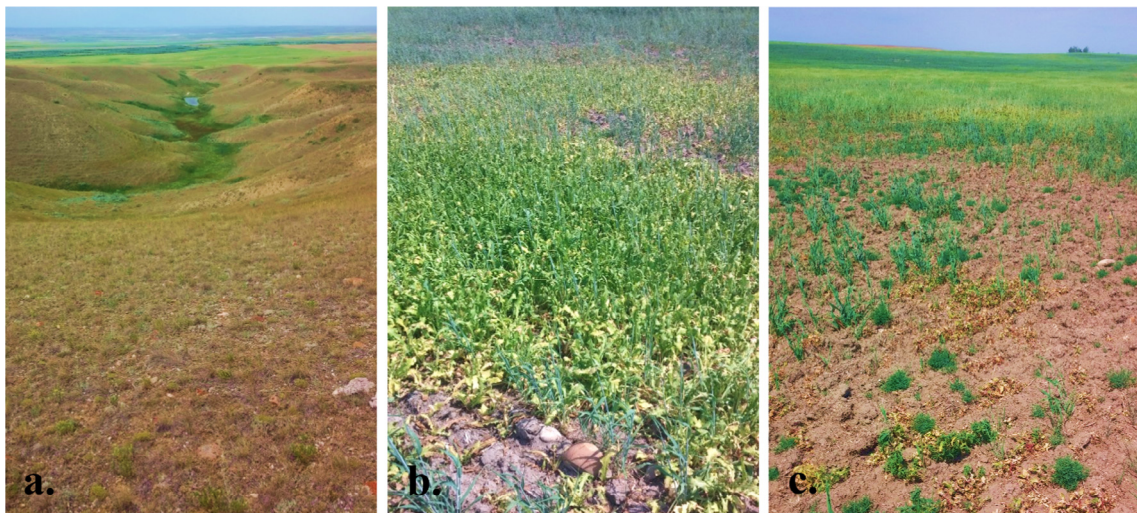


Fig. 10. Photographs of areas seen as anomalies in Fig. 9. a: Gullies and surrounding grassland showing greener vegetation near the water at the bottom of the gullies. b: An example patch of weeds located in Field 3. c: Stunted crops and sporadic vegetation throughout Field 3.

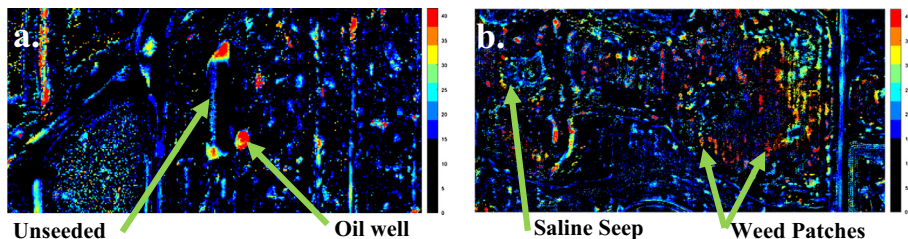


Fig. 11. Examples of identifiable anomalous areas in 2015 data. Red/orange areas are more anomalous than blue/black areas. a: An oil well causing barren soil around it and an unseeded region are both anomalous in an otherwise uniformly planted barley field. b: A barley field with a saline seep and numerous weed patches throughout.

The unseeded region near the oil well is seen to disappear (shown as green in Fig. 13) with the exception of a small area in the center that appeared in the 2016 data (shown in red). This area can also be identified as a much smaller unseeded area. This appearance is again related to comparing a fallow area against a

lush green crop; however, it also shows a weakness to simply examining the difference between data sets.

An alternative means of displaying and working with the data is to define an anomaly cutoff for each data set individually. The working definition was that any pixel with a total MAD greater

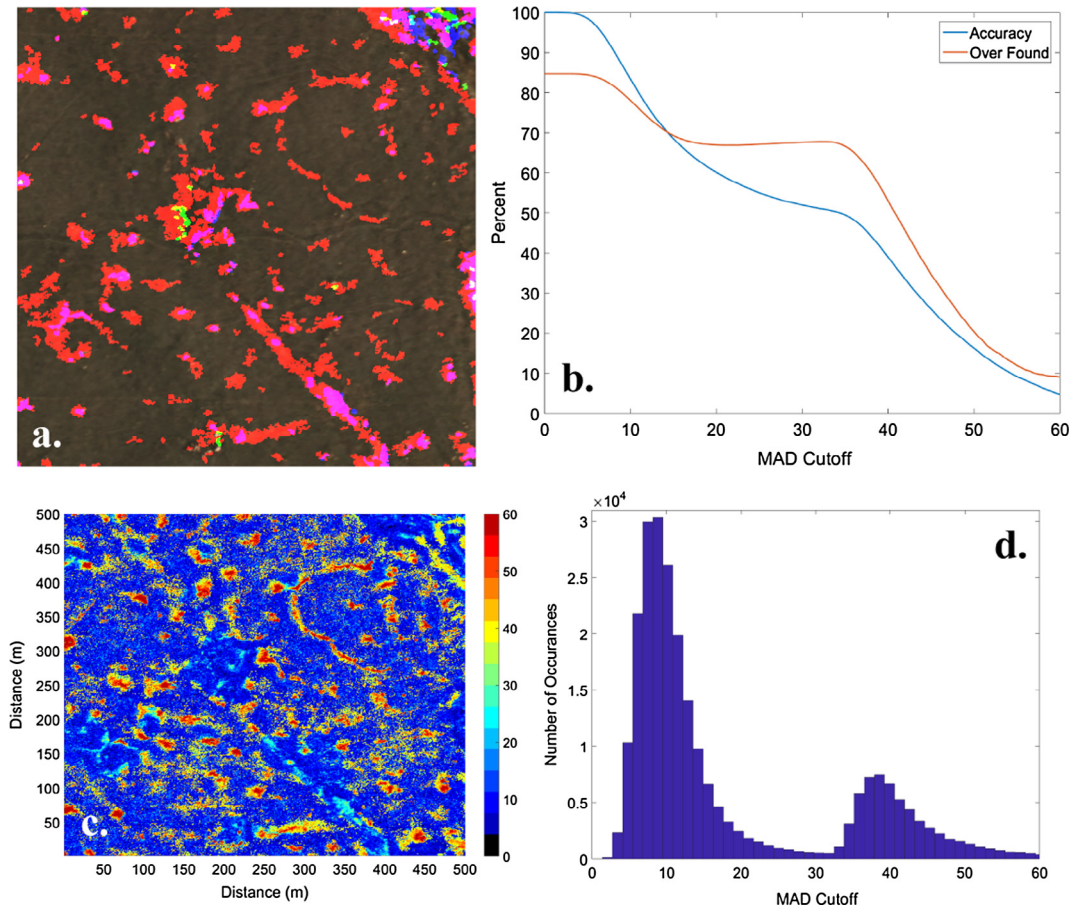


Fig. 12. 500 × 500 m area of state land consisting primarily of grasses with small bushes and rock outcrops throughout. These bushes and rocks outcrops are labeled as anomalies in 12a along with shallow gully features and boundaries of seasonal ponds. Anomalies are visualized as: red, areas higher in the visible; green, areas higher in the green region; and blue, shifted red edge. 12b shows the accuracy of the MAD method in finding the anomalies in 12a as well as the percent of the anomalies found by the MAD method that are not considered anomalies in 12a. 12c shows the number of MADs each individual pixel varies from its 41 × 41 surrounding pixel area. 12d is a histogram of occurrences of MAD values shown in 12c.

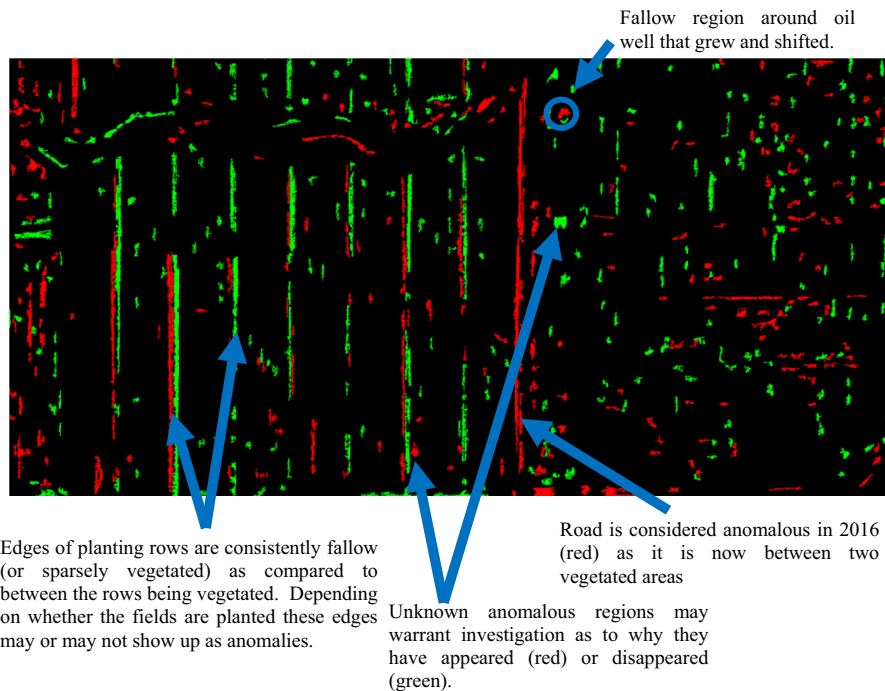


Fig. 13. Anomaly change map from 2015 and 2016. Persistent features whose local environment changes, such as the road, are seen as anomalies but there are large areas that do not have simple explanations.

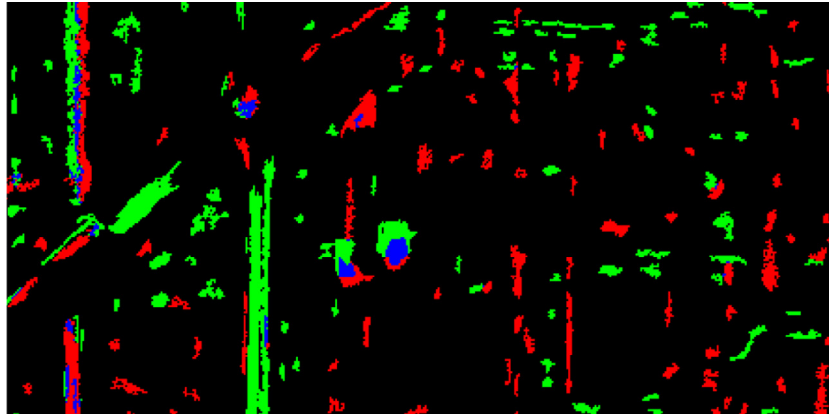


Fig. 14. Display of anomalies determined from individual data sets. Red are anomalies only seen in 2015 data, green only in 2016, and blue are anomalies seen in both sets of data.



Fig. 15. Example of developed area (a farmhouse and outbuildings). 15a is an anomaly map from 2015 (like Fig. 11). 15b is an image taken from Google Earth. 15c is like Fig. 14 showing areas which were anomalous in 2015 (red), 2016 (green), and both (blue). (For interpretation of the references to colour in this figure legend, the reader is referred to the web version of this article.)

than 20 was considered anomalous (this corresponds to twice the mean MAD across the entire image). In Fig. 14, red areas are anomalies in the 2015 as seen earlier, green areas are anomalies in the 2016 data set, and blue are areas that were anomalous in both years. By displaying the data this way, it is easier to see how the spatial extent of the oil well appears to have changed, but more so it shows the anomalies due to unseeded regions more clearly. Displaying the data in in this way also shows how persistent anomalies may be subtly changing and the effects of spatial registration.

One final qualitative example of the technique as applied to manmade structures is shown in Fig. 15. While the data collection was focused on agricultural areas one homestead was present near the edges of the collection area and serves as an example of detecting manmade structures. Further optimization would need to be done urban environment including a different pixel area as it was not necessarily optimized for determining buildings. Despite this shortcoming, most of the buildings on the farm were detected as anomalies as seen when comparing 15a (anomaly map) to 15b (Google Earth image). The smaller buildings are detected as being more anomalous due to the pixel area used. Furthermore, the buildings were detected as anomalies near the trees and the trees were detected as anomalies as well. Unfortunately, the data from 2016 had gaps due to camera recording errors that caused calibration issues that in turn contributed to the regions near the left side of the image to not have anomalies detected. Fig. 15c shows agreement between the years is excellent in the center of the image, but has disagreement due to spatial registration on the road on the right and as mentioned the left side had issues with anomaly detection in the 2016 data. Even with these deficiencies this shows the potential of the technique in urban environments.

4. Conclusions

An inexpensive hyperspectral system that can be flown on small aircraft at variable intervals allows for collection of mesoscale radiometrically referenced data even over area with no access to place spatial/spectral reference targets. These data can be used to answer a wide range of scientific questions, but this study was centered on the idea of extending the idea of detecting anomalies that can be associated with vegetation stress as a means of detecting a CO₂ leak from a sequestration site. Despite there being no CO₂ leak present, controlled or otherwise, it was possible to use the hyperspectral data to detect local anomalies within a single data set as well as to compare multiple data sets to remove persistent anomalies and detect new anomalies. While the cause of these anomalies could not be investigated, some can be explained with knowledge of the area obtained from aerial/satellite imagery and show the potential of the technique. Using aerial/satellite imagery as a means of verification the MAD technique found between 50–70% of the anomalies, with the largest source of error being related to large anomalous areas in the aerial/satellite imagery not being considered anomalies by the MAD technique.

Both the MAD based anomaly detection technique and the histogram based classification technique are examples of techniques that are improved with radiometrically referenced data. These tools can be used to further work based on as series of measurements over a period of time, and the use of radiometrically referenced data allows for quantitative comparison between data sets that might not otherwise be possible for land coverage/usage change, or disease spread, or monitoring urban expansion, etc. Over shorter time periods having radiometrically referenced data allows for more rigorous crop monitoring or effects of mesoscale environmental differences on plant growth, and many other applications.

Acknowledgements

This material is based upon work supported by the U.S. Department of Energy and the National Energy Technology Laboratory under Award Number DE-FC26-05NT42587. This report was prepared as an account of work sponsored by an agency of the United States Government. Neither the United States Government nor any agency thereof, nor any of their employees, makes any warranty, express or implied, or assumes any legal liability or responsibility for the accuracy, completeness, or usefulness of any information, apparatus, product, or process disclosed, or represents that its use would not infringe privately owned rights. Reference herein to any specific commercial product, process, or service by trade name, trademark, manufacturer, or otherwise does not necessarily constitute or imply its endorsement, recommendation, or favoring by the United States Government or any agency thereof. The views and opinions of authors expressed herein do not necessarily state or reflect those of the United States Government or any agency thereof.

References

- Apan, A., Held, A., Phinn, S., Markley, J., 2004. Detecting sugarcane 'orange rust' disease using EO-1 Hyperion hyperspectral imagery. *Int. J. Remote Sens.* 25 (2), 489–498.
- Bateson, L., Vellico, M., Beaubien, S.E., Pearce, J.M., Annunziatellis, A., Ciotoli, G., Marsh, S., 2008. The application of remote-sensing techniques to monitor CO₂-storage sites for surface leakage: method development and testing at Latera (Italy) where naturally produced CO₂ is leaking to the atmosphere. *Int. J. Greenhouse Gas Control* 2 (3), 388–400.
- Behmann, J., Steinrücken, J., Plümer, L., 2014. Detection of early plant stress responses in hyperspectral images. *ISPRS J. Photogram. Remote Sens.* 93, 98–111.
- Bellante, G.J., Powell, S.L., Lawrence, R.L., Repasky, K.S., Dougher, T.A.O., 2013. Aerial detection of a simulated CO₂ leak from a geologic sequestration site using hyperspectral imagery. *Int. J. Greenhouse Gas Control* 13, 124–137.
- Benson, S.M., Gasperikova, E., Hoversten, G.M., 2004. Monitoring protocols and life-cycle costs for geologic storage of carbon dioxide. In: *Proceedings of the 7th International Conference on Greenhouse Gas Control Technologies (GHGT-7)*, pp. 1259–1266.
- Bergfeld, D., Evans, W.C., Howle, J.F., Farrar, C.D., 2006. Carbon dioxide emissions from vegetation-kill zones around the resurgent dome of Long Valley caldera, eastern California, USA. *J. Volcanol. Geoth. Res.* 152 (1), 140–156.
- Byrne, G.F., Crapper, P.F., Mayo, K.K., 1980. Monitoring land-cover change by principal component analysis of multitemporal Landsat data. *Remote Sens. Environ.* 10 (3), 175–184.
- Carter, G.A., 1991. Primary and secondary effects of water content on the spectral reflectance of leaves. *Am. J. Bot.* 78, 916–924.
- Carter, G.A., Mitchell, R.J., Chappelka, A.H., Brewer, C.H., 1992. Response of leaf spectral reflectance in loblolly pine to increased atmospheric ozone and precipitation acidity. *J. Exp. Bot.* 43 (4), 577–584.
- Carter, G.A., Young, D.R., 1993. Foliar spectral reflectance and plant stress on a barrier island. *Int. J. Plant Sci.* 298–305.
- Carter, G.A., Knapp, A.K., 2001. Leaf optical properties in higher plants: linking spectral characteristics to stress and chlorophyll concentration. *Am. J. Bot.* 88 (4), 677–684.
- Chapin, F.S., 1991. Integrated responses of plants to stress. *Bioscience* 41 (1), 29–36.
- Conese, C., Maselli, F., 1991. Use of multitemporal information to improve classification performance of TM scenes in complex terrain. *ISPRS J. Photogram. Remote Sens.* 46 (4), 187–197.
- Cortis, A., Oldenburg, C.M., Benson, S.M., 2008. The role of optimality in characterizing CO₂ seepage from geologic carbon sequestration sites. *Int. J. Greenhouse Gas Control* 2 (4), 640–652.
- Cuffey, K.M., Vimeux, F., 2001. Covariation of carbon dioxide and temperature from the Vostok ice core after deuterium-excess correction. *Nature* 412 (6846), 523–527.
- Demirel, N., Emil, M.K., Duzgun, H.S., 2011. Surface coal mine area monitoring using multi-temporal high-resolution satellite imagery. *Int. J. Coal Geol.* 86 (1), 3–11.
- Dobrowski, S.Z., Pushnik, J.C., Zarco-Tejada, P.J., Ustin, S.L., 2005. Simple reflectance indices track heat and water stress-induced changes in steady-state chlorophyll fluorescence at the canopy scale. *Remote Sens. Environ.* 97 (3), 403–414.
- Eitel, J.U., Vierling, L.A., Litvak, M.E., Long, D.S., Schulthess, U., Ager, A.A., Stoscheck, L., 2011. Broadband, red-edge information from satellites improves early stress detection in a New Mexico conifer woodland. *Remote Sens. Environ.* 115 (12), 3640–3646.
- Feitosa, R.Q., Costa, G.A., Mota, G.L., Pakzad, K., Costa, M.C., 2009. Cascade multitemporal classification based on fuzzy Markov chains. *ISPRS J. Photogram. Remote Sens.* 64 (2), 159–170.
- Franke, J., Menz, G., 2007. Multi-temporal wheat disease detection by multi-spectral remote sensing. *Precision Agric.* 8 (3), 161–172.
- Gevaert, C.M., Suomalainen, J., Tang, J., Kooistra, L., 2015. Generation of Spectral-Temporal Response Surfaces by Combining Multispectral Satellite and Hyperspectral UAV Imagery for Precision Agriculture Applications. *IEEE J. Select. Top. Appl. Earth Observ. Remote Sens.* 8 (6), 3140–3146.
- Goenaga, M.A., Torres-Madroneo, M.C., Velez-Reyes, M., Van Bloem, S.J., China, J.D., 2013. Unmixing analysis of a time series of Hyperion images over the Guánica dry forest in Puerto Rico. *IEEE J. Select. Top. Appl. Earth Observ. Remote Sens.* 6 (2), 329–338.
- Gomez-Chova, L., Fernández-Prieto, D., Calpe, J., Soria, E., Vila, J., Camps-Valls, G., 2006. Urban monitoring using multi-temporal SAR and multi-spectral data. *Pattern Recogn. Lett.* 27 (4), 234–243.
- Hadjimitsis, D.G., Clayton, C.R.I., Retalis, A., 2009. The use of selected pseudo-invariant targets for the application of atmospheric correction in multi-temporal studies using satellite remotely sensed imagery. *Int. J. Appl. Earth Obs. Geoinf.* 11 (3), 192–200.
- Hemissi, S., Farah, I.R., Etabaa, K.S., Solaiman, B., 2013. Multi-spectro-temporal analysis of hyperspectral imagery based on 3-D spectral modeling and multilinear algebra. *IEEE Trans. Geosci. Remote Sens.* 51 (1), 199–216.
- Hong, S.H., Wdowinski, S., Kim, S.W., Won, J.S., 2010. Multi-temporal monitoring of wetland water levels in the Florida Everglades using interferometric synthetic aperture radar (InSAR). *Remote Sens. Environ.* 114 (11), 2436–2447.
- Howell, D.C., 2014. Median Absolute Deviation. *Wiley StatsRef: Statistics Reference Online*.
- Jones, C.L., Weckler, P.R., Maness, N.O., Stone, M.L., Jayasekara, R., 2004. Estimating water stress in plants using hyperspectral sensing. In: *2004 ASAE Annual Meeting. American Society of Agricultural and Biological Engineers*, p. 1.
- Keith, C.J., Repasky, K.S., Lawrence, R.L., Jay, S.C., Carlsten, J.L., 2009. Monitoring effects of a controlled subsurface carbon dioxide release on vegetation using a hyperspectral imager. *Int. J. Greenhouse Gas Control* 3 (5), 626–632.
- Kerekes, J., Muldowney, M., Strackerjan, K., Smith, L., Leahy, B., 2006. Vehicle tracking with multi-temporal hyperspectral imagery. In: *Defense and Security Symposium. International Society for Optics and Photonics*, pp. 62330C–62330C.
- Kim, Y., Glenn, D.M., Park, J., Ngugi, H.K., Lehman, B.L., 2011. Hyperspectral image analysis for water stress detection of apple trees. *Comput. Electron. Agricult.* 77 (2), 155–160.
- Knauss, K.G., Johnson, J.W., Steefel, C.I., 2005. Evaluation of the impact of CO₂, co-contaminant gas, aqueous fluid and reservoir rock interactions on the geologic sequestration of CO₂. *Chem. Geol.* 217 (3), 339–350.
- Knipling, E.B., 1970. Physical and physiological basis for the reflectance of visible and near-infrared radiation from vegetation. *Remote Sens. Environ.* 1 (3), 155–159.
- Korbøl, R., Kaddour, A., 1995. Sleipner vest CO₂ disposal-injection of removed CO₂ into the Utsira formation. *Energy Convers. Manage.* 36 (6), 509–512.
- Lausch, A., Pause, M., Schmidt, A., Salbach, C., Gwilym-Margianto, S., Merbach, I., 2013. Temporal hyperspectral monitoring of chlorophyll, LAI, and water content of barley during a growing season. *Can. J. Remote. Sens.* 39 (3), 191–207.
- Lays, C., Ley, C., Klein, O., Bernard, P., Licata, L., 2013. Detecting outliers: do not use standard deviation around the mean, use absolute deviation around the median. *J. Exp. Soc. Psychol.* 49 (4), 764–766.
- Li, L., Ustin, S.L., Lay, M., 2005. Application of AVIRIS data in detection of oil-induced vegetation stress and cover change at Jornada, New Mexico. *Remote Sens. Environ.* 94 (1), 1–16.
- Li, X., Yeh, A.G.O., 1998. Principal component analysis of stacked multi-temporal images for the monitoring of rapid urban expansion in the Pearl River Delta. *Int. J. Remote Sens.* 19 (8), 1501–1518.
- Li, Z., Dong, M., Li, S., Huang, S., 2006. CO₂ sequestration in depleted oil and gas reservoirs—caprock characterization and storage capacity. *Energy Convers. Manage.* 47 (11), 1372–1382.
- Liangyun, L., Mui, H., Wenjiang, H., 2004. Monitoring stripe rust disease of winter wheat using multi-temporal hyperspectral airborne data. *J. Remote Sens.* 8 (3), 275–281.
- Liu, D., Kelly, M., Gong, P., 2006. A spatial-temporal approach to monitoring forest disease spread using multi-temporal high spatial resolution imagery. *Remote Sens. Environ.* 101 (2), 167–180.
- Liu, J., Pattey, E., Miller, J.R., McNairn, H., Smith, A., Hu, B., 2010. Estimating crop stresses, aboveground dry biomass and yield of corn using multi-temporal optical data combined with a radiation use efficiency model. *Remote Sens. Environ.* 114 (6), 1167–1177.
- Lucas, R., Rowlands, A., Brown, A., Keyworth, S., Bunting, P., 2007. Rule-based classification of multi-temporal satellite imagery for habitat and agricultural land cover mapping. *ISPRS J. Photogram. Remote Sens.* 62 (3), 165–185.
- Lunetta, R.S., Knight, J.F., Ediriwickrema, J., Lyon, J.G., Worthy, L.D., 2006. Land-cover change detection using multi-temporal MODIS NDVI data. *Remote Sens. Environ.* 105 (2), 142–154.
- Luther, J.E., Carroll, A.L., 1999. Development of an index of balsam fir vigor by foliar spectral reflectance. *Remote Sens. Environ.* 69 (3), 241–252.
- Maček, I., Pfanz, H., Francetič, V., Batič, F., Vodnik, D., 2005. Root respiration response to high CO₂ concentrations in plants from natural CO₂ springs. *Environ. Exp. Bot.* 54 (1), 90–99.
- Makki, I., Younes, R., Francis, C., Bianchi, T., Zucchetti, M., 2017. A survey of landmine detection using hyperspectral imaging. *ISPRS J. Photogram. Remote Sens.* 124, 40–53.

- Maktav, D., Erbek, F.S., 2005. Analysis of urban growth using multi-temporal satellite data in Istanbul, Turkey. *Int. J. Remote Sens.* 26 (4), 797–810.
- Maldal, T., Tappel, I.M., 2004. CO₂ underground storage for S_{no}hvit gas field development. *Energy* 29 (9), 1403–1411.
- Male, E.J., Pickles, W.L., Silver, E.A., Hoffmann, G.D., Lewicki, J., Apple, M., Burton, E. A., 2010. Using hyperspectral plant signatures for CO₂ leak detection during the 2008 ZERT CO₂ sequestration field experiment in Bozeman, Montana. *Environ. Earth Sci.* 60 (2), 251–261.
- Mallet, C., Chehata, N., Mercier, G., 2015. Theme issue “Multitemporal remote sensing data analysis”. *ISPRS J. Photogram. Remote Sens.* 107, 1–2.
- McCann, C., Repasky, K.S., Morin, M., Lawrence, R.L., Powell, S., 2017a. Using landsat surface reflectance data as a reference target for multiswath hyperspectral data collected over mixed agricultural rangeland areas. *IEEE Trans. Geosci. Remote Sens.*
- McCann, C., Repasky, K.S., Morin, M., Lawrence, R.L., Powell, S., 2017b. Novel histogram based unsupervised classification technique to determine natural classes from biophysically relevant fit parameters to hyperspectral data. *IEEE J. Select. Top. Appl. Earth Observ. Remote Sens.* 1–11. <http://dx.doi.org/10.1109/jstars.2017.2701360>.
- Monnin, E., Indermühle, A., Dällenbach, A., Flückiger, J., Stauffer, B., Stocker, T.F., Barnola, J.M., 2001. Atmospheric CO₂ concentrations over the last glacial termination. *Science* 291 (5501), 112–114.
- Nguyen, H.T., Lee, B.W., 2006. Assessment of rice leaf growth and nitrogen status by hyperspectral canopy reflectance and partial least square regression. *Eur. J. Agron.* 24 (4), 349–356.
- Noomen, M.F., Skidmore, A.K., 2009. The effects of high soil CO₂ concentrations on leaf reflectance of maize plants. *Int. J. Remote Sens.* 30 (2), 481–497.
- Noomen, M.F., Smith, K.L., Colls, J.J., Steven, M.D., Skidmore, A.K., Van Der Meer, F.D., 2008. Hyperspectral indices for detecting changes in canopy reflectance as a result of underground natural gas leakage. *Int. J. Remote Sens.* 29 (20), 5987–6008.
- Oldenburg, C.M., Bryant, S.L., Nicot, J.P., 2009. Certification framework based on effective trapping for geologic carbon sequestration. *Int. J. Greenhouse Gas Control* 3 (4), 444–457.
- Ong, C., Cudahy, T., 2002. Deriving quantitative monitoring data related to acid drainage using multi-temporal hyperspectral data. In: *AVIRIS Workshop*.
- Pachauri, R.K., Reisinger, A., 2007. IPCC Fourth Assessment Report. IPCC, Geneva.
- Petit, J.R., Jouzel, J., Raynaud, D., Barkov, N.I., Barnola, J.M., Basile, I., Delmotte, M., 1999. Climate and atmospheric history of the past 420,000 years from the Vostok ice core, Antarctica. *Nature* 399 (6735), 429–436.
- Petitjean, F., Kurtz, C., Passat, N., Gançarski, P., 2012. Spatio-temporal reasoning for the classification of satellite image time series. *Pattern Recogn. Lett.* 33 (13), 1805–1815.
- Pickles, W., Cover, W., 2004. Hyperspectral geobotanical remote sensing for CO₂ storage monitoring (No. UCRL-BOOK-204165). Lawrence Livermore National Laboratory (LLNL), Livermore, CA.
- Pruess, K., 2008. On CO₂ fluid flow and heat transfer behavior in the subsurface, following leakage from a geologic storage reservoir. *Environ. Geol.* 54 (8), 1677–1686.
- Rogan, J., Franklin, J., Roberts, D.A., 2002. A comparison of methods for monitoring multitemporal vegetation change using Thematic Mapper imagery. *Remote Sens. Environ.* 80 (1), 143–156.
- Rutqvist, J., Vasco, D.W., Myer, L., 2010. Coupled reservoir-geomechanical analysis of CO₂ injection and ground deformations at In Salah, Algeria. *Int. J. Greenhouse Gas Control* 4 (2), 225–230.
- Siegenthaler, U., Stocker, T.F., Monnin, E., Lüthi, D., Schwander, J., Stauffer, B., Jouzel, J., 2005. Stable carbon cycle–climate relationship during the late Pleistocene. *Science* 310 (5752), 1313–1317.
- Smith, K.L., Steven, M.D., Colls, J.J., 2004. Use of hyperspectral derivative ratios in the red-edge region to identify plant stress responses to gas leaks. *Remote Sens. Environ.* 92 (2), 207–217.
- Somers, B., Asner, G.P., 2012. Hyperspectral time series analysis of native and invasive species in Hawaiian rainforests. *Remote Sens.* 4 (9), 2510–2529.
- Somers, B., Asner, G.P., 2013. Multi-temporal hyperspectral mixture analysis and feature selection for invasive species mapping in rainforests. *Remote Sens. Environ.* 136, 14–27.
- Spangler, L.H., Dobeck, L.M., Repasky, K.S., Nehrir, A.R., Humphries, S.D., Barr, J.L., Benson, S.M., 2010. A shallow subsurface controlled release facility in Bozeman, Montana, USA, for testing near surface CO₂ detection techniques and transport models. *Environ. Earth Sci.* 60 (2), 227–239.
- Strachan, I.B., Pattey, E., Boisvert, J.B., 2002. Impact of nitrogen and environmental conditions on corn as detected by hyperspectral reflectance. *Remote Sens. Environ.* 80 (2), 213–224.
- Strazisar, B.R., Wells, A.W., Diehl, J.R., Hammack, R.W., Veloski, G.A., 2009. Near-surface monitoring for the ZERT shallow CO₂ injection project. *Int. J. Greenhouse Gas Control* 3 (6), 736–744.
- Stuckens, J., Dzikiti, S., Verstraeten, W.W., Verreyne, S., Swennen, R., Coppin, P., 2011. Physiological interpretation of a hyperspectral time series in a citrus orchard. *Agric. For. Meteorol.* 151 (7), 1002–1015.
- Suárez, L., Zarco-Tejada, P.J., Sepulcre-Cantó, G., Pérez-Priego, O., Miller, J.R., Jiménez-Muñoz, J.C., Sobrino, J., 2008. Assessing canopy PRI for water stress detection with diurnal airborne imagery. *Remote Sens. Environ.* 112 (2), 560–575.
- Travelletti, J., Delacourt, C., Allemand, P., Malet, J.P., Schmittbuhl, J., Toussaint, R., Bastard, M., 2012. Correlation of multi-temporal ground-based optical images for landslide monitoring: application, potential and limitations. *ISPRS J. Photogram. Remote Sens.* 70, 39–55.
- Tripathy, G.K., Ghosh, T.K., Shah, S.D., 1996. Monitoring of desertification process in Karnataka state of India using multi-temporal remote sensing and ancillary information using GIS. *Int. J. Remote Sens.* 17 (12), 2243–2257.
- Tilling, A.K., O’Leary, G.J., Ferwerda, J.G., Jones, S.D., Fitzgerald, G.J., Rodriguez, D., Belford, R., 2007. Remote sensing of nitrogen and water stress in wheat. *Field Crops Res.* 104 (1), 77–85.
- Wells Search. Retrieved February 20, 2017. <<http://www.bogc.dnrc.mt.gov/webapps/dataminer/Wells/Wells.aspx>>.
- Whittaker, S.G., 2004. Geological storage of greenhouse gases: the IEA Weyburn CO₂ monitoring and storage project. *Can. Soc. Petrol. Geologists Reserv.* 31 (8), 9.
- Wilson, E.J., Friedmann, S.J., Pollak, M.F., 2007. Research for deployment: incorporating risk, regulation, and liability for carbon capture and sequestration. *Environ. Sci. Technol.* 41 (17), 5945–5952.
- Xian, G., Crane, M., McMahon, C., 2008. Quantifying multi-temporal urban development characteristics in Las Vegas from Landsat and ASTER data. *Photogram. Eng. Remote Sens.* 74 (4), 473–481.
- Xie, C.Q., Li, X.L., Nie, P.C., He, Y., 2013. Application of time series hyperspectral imaging (TS-HSI) for determining water content within tea leaves during drying. *Trans. ASABE* 56, 1431–1440.
- Yuan, D., Elvidge, C.D., 1996. Comparison of relative radiometric normalization techniques. *ISPRS J. Photogram. Remote Sens.* 51 (3), 117–126.
- Yuan, Y., Lv, H., Lu, X., 2015. Semi-supervised change detection method for multi-temporal hyperspectral images. *Neurocomputing* 148, 363–375.
- Zarco-Tejada, P.J., Ustin, S.L., Whiting, M.L., 2005. Temporal and spatial relationships between within-field yield variability in cotton and high-spatial hyperspectral remote sensing imagery. *Agron. J.* 97 (3), 641–653.
- Zhang, Q., Wang, J., Peng, X., Gong, P., Shi, P., 2002. Urban built-up land change detection with road density and spectral information from multi-temporal Landsat TM data. *Int. J. Remote Sens.* 23 (15), 3057–3078.
- Zhang, M., Qin, Z., Liu, X., Ustin, S.L., 2003. Detection of stress in tomatoes induced by late blight disease in California, USA, using hyperspectral remote sensing. *Int. J. Appl. Earth Obs. Geoinf.* 4 (4), 295–310.
- Zhao, C., Liu, L., Wang, J., Huang, W., Song, X., Li, C., 2005. Predicting grain protein content of winter wheat using remote sensing data based on nitrogen status and water stress. *Int. J. Appl. Earth Obs. Geoinf.* 7 (1), 1–9.
- Zhao, R., Du, B., Zhang, L., Zhang, L., 2016. A robust background regression based score estimation algorithm for hyperspectral anomaly detection. *ISPRS J. Photogram. Remote Sens.* 122, 126–144.